PHYSICAL REVIEW B **96**, 014414 (2017)

Quantum critical phase with infinite projected entangled paired states

Didier Poilblanc and Matthieu Mambrini
Laboratoire de Physique Théorique, C.N.R.S. and Université de Toulouse, 31062 Toulouse, France
(Received 1 March 2017; published 12 July 2017)

A classification of SU(2)-invariant projected entangled paired states (PEPS) on the square lattice, based on a unique site tensor, has been recently introduced by Mambrini *et al.* [M. Mambrini, R. Orús, and D. Poilblanc, Phys. Rev. B **94**, 205124 (2016)]. It is not clear whether such SU(2)-invariant PEPS can either (i) exhibit long-range magnetic order (such as in the Néel phase) or (ii) describe a genuine quantum critical point (QCP) or quantum critical phase (QCPh) separating two ordered phases. Here, we identify a specific family of SU(2)-invariant PEPS of the classification which provides excellent variational energies for the $J_1 - J_2$ frustrated Heisenberg model, especially at $J_2 = 0.5$, corresponding to the approximate location of the QCP or QCPh separating the Néel phase from a dimerized phase. The PEPS are built from virtual states belonging to the $\frac{1}{2}^{\otimes N} \oplus 0$ SU(2) representation, i.e., with N "colors" of virtual spin-$\frac{1}{2}$. Using a full-update infinite-PEPS approach directly in the thermodynamic limit, based on the corner transfer matrix renormalization algorithm supplemented by a conjugate gradient optimization scheme, we provide evidence of (i) the absence of magnetic order and of (ii) diverging correlation lengths (i.e., showing no sign of saturation with increasing environment dimension) in both the singlet and triplet channels, when the number of colors $N \geqslant 3$. We argue that such a PEPS gives a qualitative description of the QCP or QCPh of the $J_1 - J_2$ model.

DOI: 10.1103/PhysRevB.96.014414

I. INTRODUCTION

Low-dimensional quantum magnets offer a rich zoo of phases breaking a discrete (such as point-group or lattice) or a continuous (such as spin-rotation) symmetry. Often, such phases are separated by quantum critical points (QCP), as described within the usual Ginsburg-Landau (GL) framework. Interestingly, it has been proposed that some QCP may *not* be described by the GL paradigm [1,2]. A celebrated quantum spin model is the frustrated spin-$\frac{1}{2}$ Heisenberg model on the two-dimensional (2D) square lattice involving competition between nearest-neighbor (NN) and next-nearest-neighbor (NNN) antiferromagnetic (AF) couplings, J_1 and J_2, respectively. Setting $J_1 = 1$, J_2 controls the amount of frustration which is maximum (classically) at $J_2 = 0.5$. Large-scale quantum Monte Carlo (QMC) simulations [3–5] have shown that the ground state (GS) of the unfrustrated ($J_2 = 0$) Heisenberg model exhibits long-range (LR) AF order. In the thermodynamic limit, the (global) spin-rotational SU(2) symmetry is spontaneously broken and the GS acquires a finite local staggered magnetization. When J_2 is turned on, the order parameter is gradually suppressed and a quantum phase transition to a quantum disordered (QD) phase [6–9]—such as a dimer [10–13] or a plaquette [14,15] valence bond crystal (VBC)—takes place (see Fig. 1). It was also argued that magnetic frustration could stabilize spin liquids (with no symmetry breaking), such as the resonating valence bond (RVB) states [16] showing algebraic (short-range) VBC correlations on the square (kagome) lattice [17–20].

Recently, tremendous progress have been made in tensor network techniques [22–26], aiming to go beyond density matrix renormalization-group (DMRG) methods [27] in 2D. More specifically, projected entangled pair states (PEPS) [28] are variational Ansätze constructed from a few local tensors, located on M nonequivalent sites, and characterized by (i) one bond carrying the physical degrees of freedom (of dimension 2 for spin-$\frac{1}{2}$ systems) and (ii) z "virtual" bonds (z is the lattice coordination number, $z = 4$ for the square lattice) of arbitrary dimension D, as shown in Fig. 2(a). Interestingly, any local (gauge) or global (physical) symmetry can be implemented in PEPS [29–37]. Also, a simple bulk-edge (holographic) correspondence provides a remarkable tool to investigate the properties of edge states [38,39]. Many remarkable states of matter such as trivial paramagnets [40], topological [19,20,41] or algebraic [19] RVB spin liquids, loop spin liquids [42], superfluids [43], or unconventional correlated superconductors [44] have simple representations in terms of PEPS. Numerical calculations with PEPS do not require one to compute the wave-function coefficients (which, conceptually, are given by contracting the tensor network over all virtual links) but, rather, make use of transfer matrices [45] based on "double-layer" tensors [see Figs. 2(b)–2(e)]. In the infinite-PEPS (iPEPS) method [46], one works directly in the thermodynamic limit by approximating the (infinite) space around a small M-site cluster by an effective "environment" [see Fig. 2(f)]. One of the most accurate computations of the environment is based on a renormalization-group scheme involving corner transfer matrices (CTMRG) [47–50], as shown in Figs. 2(g) and 2(h). Unrestricted energy minimization over the MdD^z tensor coefficients can be performed using time evolution block decimation (TEBD) [51,52], which has to be combined with a simple update [53,54] or a full update [55] of the environment. A (finite) PEPS method using a 2×2 cluster update supplemented by a finite-size extrapolation has also been introduced [56]. Recently, a new optimization scheme using a conjugate gradient (CG) algorithm has been tested on the nonfrustrated [57,58] and frustrated [59] Heisenberg model, with iPEPS or finite PEPS, respectively.

The entanglement entropy (i.e., the quantity measuring the amount of entanglement in a bipartitioned system) in a spontaneously broken state exhibits anomalous additive logarithmic corrections [60–62] to the area law (i.e., the linear scaling of the entropy with the length of the cut). When the staggered magnetization $m_{\text{stag}} \to 0$, at the QCP, the violation of the area law is expected to be even more severe. This means

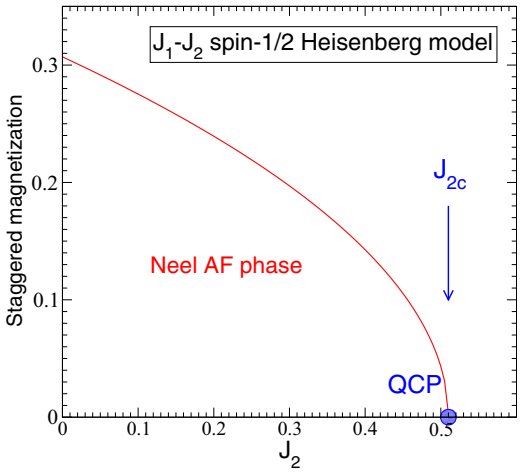

FIG. 1. Schematical behavior of the staggered magnetization of the spin-$\frac{1}{2}$ $J_1 - J_2$ Heisenberg model (J_1 is set to 1). $m_{\rm stag}$ vanishes at the QCP. The exact location J_{2c} of the QCP, may be close to 0.5. Recent DMRG studies [21] quote a narrow QCPh region around $J_2 = 0.5$.

that a good description of the QCP, or even of the Néel state, in terms of a PEPS (which strictly fulfills the area law for any finite D) is particularly challenging. A very simple ($D = 3$) PEPS ansatz for the Néel state on the square lattice was first proposed in terms of a (one-parameter) spinon-doped RVB phase [63]. Also, finite-size PEPS [64] or, more recently, state-of-the-art iPEPS calculations involving a conjugate gradient (CG) minimization algorithm [57,58] produced very accurate energy for the Néel GS of the 2D Heisenberg model. However, the phase diagram of the $J_1 - J_2$ model is still heavily debated. No agreement has been reached between several numerical approaches, either on the nature of the QD region—with proposals of VBC [13,15,65,66], (topological) gapped [67] or gapless [66,68–71] spin liquids—or on the location $J_2 = J_{2c}$ of the phase transition. While early exact-diagonalization (ED) extrapolations [13] were bracketing $J_{2c} \in [0.34,0.6]$, DMRG studies [66,67] suggested $J_{2c} \simeq 0.41$–0.44, while variational Monte Carlo (VMC) studies [70,71] give $J_{2c} \simeq 0.48$–0.5 and finite-size (cluster update) PEPS computations [56] $J_{2c} \simeq 0.572(5)$. Recently, Wang and Sandvik [21] argued for a quantum critical phase (QCPh) centered around 0.5. In all of these approaches (except ED), the spin-rotational SU(2) symmetry is *explicitly* broken in the Néel phase. However, there is no obstruction principle to construct accurate SU(2)-symmetric wave functions exhibiting long-range AF order [72]. Since such states may be characterized by a large entanglement, it is unclear whether it can be realized with low-D symmetric PEPS. Also, whether SU(2)-symmetric

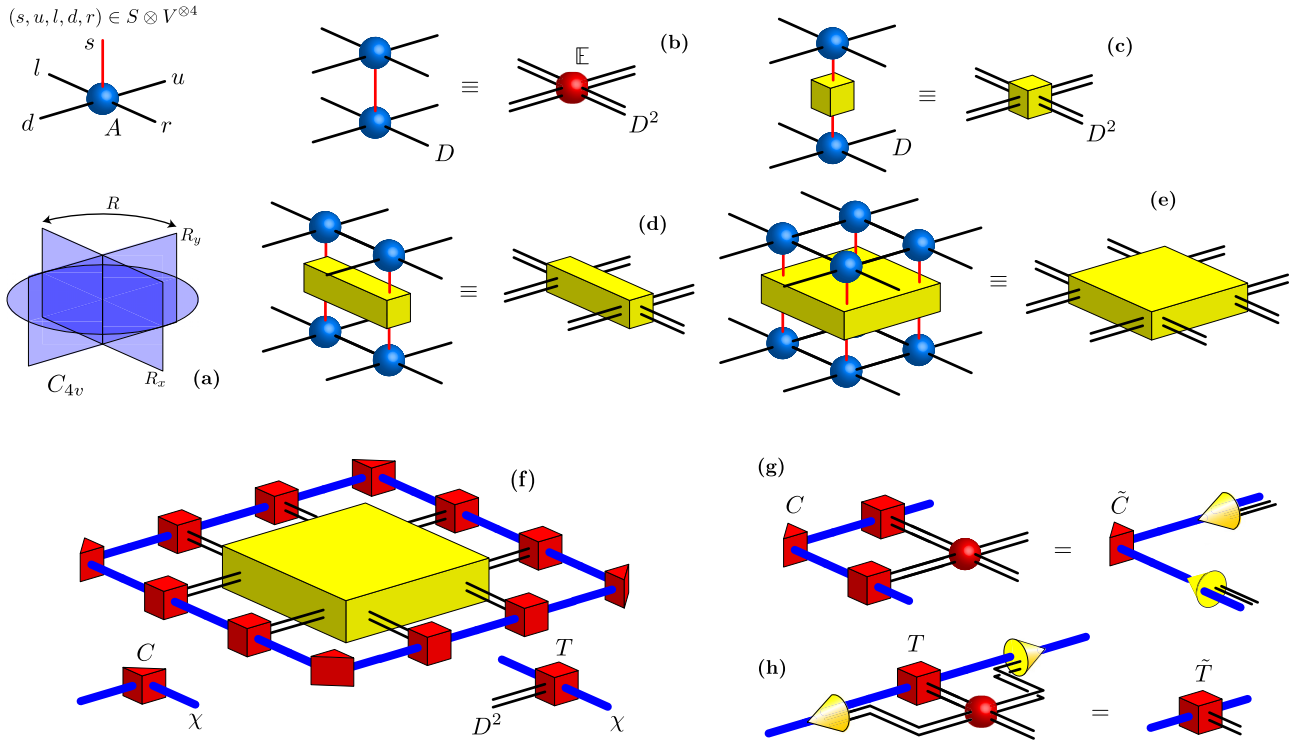

FIG. 2. (a) Symmetric PEPS tensor A with one physical index $s = \pm\frac{1}{2}$ and four virtual indices u, l, d, and r (of dimension D). A is invariant under the generators of the C_{4v} point group, i.e., the 90-degree rotation R, the reflection R_x, and the inversion $I = R_x R_y$. (b)–(e) The "two-layer" (TL) tensors have bond dimension D^2 (double lines). One-site, two-site, and four-site TL tensors obtained by inserting the identity $\mathbb{I}$, a one-site, a two-site, and a four-site operator, respectively. (f) iPEPS CTM method: a 2×2 cluster is surrounded by a (self-consistent) environment built from a corner $\chi \times \chi$ transfer matrix C and a side $\chi \times D^2 \times \chi$ tensor T. In practice, we choose $\chi = kD^2$, $k \in \mathbb{N}$. Here the operator inserted on the four-site is either $\mathbb{I}^{\otimes 4}$ (normalization) or the $J_1 - J_2$ Hamiltonian. (g) Tensor renormalization scheme: after one site is added, the new $\chi D^2 \times \chi D^2$ CTM is diagonalized and only the largest (in modulus) χ eigenvalues are kept to get the new CTM. (h) The unitaries approximated by isometries (yellow pyramids) are used to compute the new edge tensor.

PEPS have the potential to describe zero-temperature QCP or QCPh—in the same way as one-dimensional (1D) matrix product states (MPS) can describe critical 1D systems [73–75]—is still unclear [76]; although it is known that nontrivial criticality can be captured by PEPS, even at finite D [48,77].

Motivated by the above conceptual and practical issues, we have revisited the $J_1 - J_2$ model using some new PEPS developments, based on a general scheme to construct SU(2)-symmetric PEPS using computer-assisted algebra [29]. This enables us to introduce key features in the full-update iPEPS scheme: (i) Full translational and rotational invariance is enforced by using a unique SU(2)-invariant tensor on every lattice site; (ii) full optimization of the (few) tensor coefficients is accomplished via a CG method; (iii) careful scaling with environment dimension χ is performed in order to address the $\chi \to \infty$ limit. Using this procedure, we have identified a specific (low-dimensional) family of SU(2)-symmetric PEPS which provides excellent variational energies for the $J_1 - J_2$ frustrated Heisenberg model, especially at $J_2 = 0.5$, i.e., close to the (unknown) QCP or QCPh of this model. We show evidence that these (optimized) PEPS do not exhibit long-range AF order. We also find that above bond dimension $D = 7$, the PEPS (optimized for $J_2 = 0.5$) exhibits diverging spin-spin and dimer-dimer correlation lengths, i.e., showing no sign of saturation up to large environment dimension. In addition, a small spurious m_{stag} is found to vanish in the limit of infinite environment dimension. Hence, we propose that this state offers a realization of the QCP or QCPh.

II. SYMMETRIC PEPS ANSÄTZE

We wish here to consider transitionally invariant fully symmetric PEPS in order to (i) reduce the number of independent variational parameters and (ii) provide a good description of the critical point (or phase) where both SU(2) and lattice symmetries are preserved. For this purpose, we shall use the elegant classification of SU(2)-invariant PEPS tensors on the square lattice [29] according to (i) their virtual degrees of freedom and (ii) how they transform with respect to the (lattice) point-group symmetries [see Fig. 2(a)]. For simplicity, we shall *a priori* restrict ourselves to tensors that are fully invariant under all operations of the C_{4v} point group (i.e., belonging to the so-called A_1 irrep). The tensors are further classified according to their virtual space V given by a direct sum of SU(2) irrep's or "spins", i.e., $V = \bigoplus_\alpha s_\alpha$. We restrict hereafter to bond dimension $D \leqslant 7$. Among all of the possible cases listed in Table I, we focus on the most interesting ones carrying low virtual spins defined by $V = \frac{1}{2} \oplus 0\,(D = 3)$, $V = \frac{1}{2} \oplus 0 \oplus 0\,(D = 4)$, $V = 1 \oplus \frac{1}{2}\,(D = 5)$, $V = \frac{1}{2} \oplus \frac{1}{2} \oplus 0\ (D = 5)$, and $V = \frac{1}{2} \oplus \frac{1}{2} \oplus \frac{1}{2} \oplus 0\ (D = 7)$, spanned by a small number $\mathcal{D}$ of independent tensors, $\mathcal{D} = 2,8,4,10,30$, respectively, given in the Supplemental Material of Ref. [29] (except for $D = 7$ given in the Supplemental Material of this paper [78]). Note that a π rotation of the spin basis is assumed on the sites of one of the two sublattices of the square lattice. In this basis, a genuine $\mathbf{q} = \mathbf{q}_{\text{AF}} \equiv (\pi,\pi)$ (spontaneous) magnetic order translates into a *uniform* $\mathbf{q} = 0$ (spontaneous) magnetization. Subsequently, the generator of SU(2) becomes invariant only up to translations that map the sublattices to themselves (i.e., shifts over two sites).

The iPEPS method combined with full tensor optimization. We shall now focus on the $J_1 - J_2$ spin-$\frac{1}{2}$ Heisenberg model with NN and NNN antiferromagnetic coupling J_1 and J_2, respectively, which we have studied at $J_2 = 0$ in the absence of frustration and, for strong frustration, at $J_2 = 0.5$ and $J_2 = 0.55$. Our first goal is to optimize the variational energy within each $\mathcal{D}$-dimensional class of SU(2)-invariant PEPS, i.e., finding the optimum linear superposition of the $\mathcal{D}$ independent tensors of each class. Since the number of variational parameters remains small (maximum of $\mathcal{D} = 30$ for $D = 7$), we have used a "brute force" CG optimization as, e.g., given in *Numerical Recipes* [79]. However, this requires an efficient iPEPS computation of the variational energy for any set of variational parameters to "feed" the CG routine. This is performed constructing a self-consistent environment around an active 2×2 cluster [see Fig. 2(b)] using an iterative CTMRG algorithm [47,49,50] optimized for spatially symmetric tensors. Indeed, we have introduced simple modifications: (i) we use a *unique* CTM C tensor (side tensor T) which is the same for all corners (edges), and (ii) the basic singular value decomposition (SVD) in each CTMRG step to construct the environment is replaced by a (more stable) ED, with the CTM being a symmetric matrix. The largest environment dimension we could handle was $\chi = 400$ and $\chi = 294$ for $D = 5$ and $D = 7$, respectively, for which up to 350 or 400 iterations became necessary to converge the environment. Note that the initial C (T) tensor is obtained from the $\mathbb{E}$ tensor of Fig. 2(b) by summing over all external l and u (u) indices.

Energetics. Variational energies (per site) in each class of tensors are shown in Fig. 3(a) for $J_2 = 0.5$, as a function of the inverse of the environment dimension χ. A rapid

TABLE I. List of all virtual spaces V of bond dimension $D \leqslant 7$ for which $V^{\otimes 4}$ can be projected onto a physical spin-1/2. The ones considered here are indicated by (green) marks. Classes with higher spins give poorer variational energies than the lower spin ones of the same total bond dimension D.

D	3	4	5	6	7
V	✓ $\frac{1}{2} \oplus 0$	✓ $\frac{1}{2} \oplus 0 \oplus 0$	$\frac{1}{2} \oplus 0 \oplus 0 \oplus 0$ ✓ $\frac{1}{2} \oplus \frac{1}{2} \oplus 0$ ✓ $1 \oplus \frac{1}{2}$ $\frac{3}{2} \oplus 0$	$1 \oplus \frac{1}{2} \oplus 0$	✓ $\frac{1}{2} \oplus \frac{1}{2} \oplus \frac{1}{2} \oplus 0$ $1 \oplus \frac{1}{2} \oplus 0 \oplus 0$ $\frac{3}{2} \oplus \frac{1}{2} \oplus 0$ $\frac{3}{2} \oplus 1$ $2 \oplus \frac{1}{2}$ $\frac{5}{2} \oplus 0$

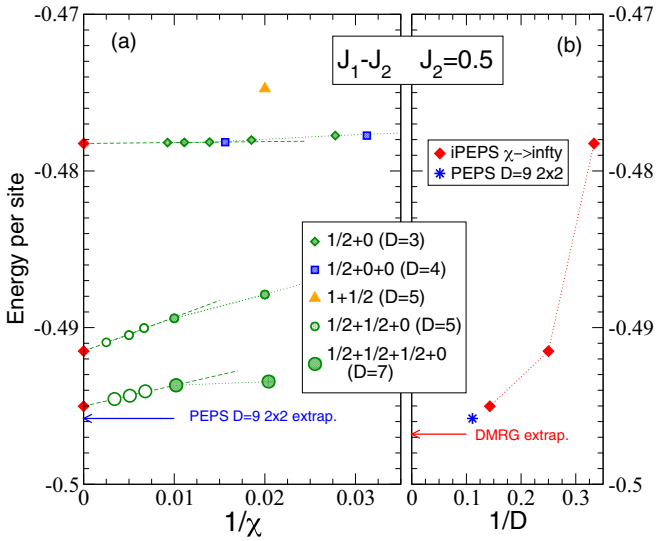

FIG. 3. (a) iPEPS variational energies of the $J_1 - J_2$ model at $J_2 = 0.5$ vs the inverse of the environment dimension χ. Full (open) symbols correspond to fully optimized (fixed) tensor Ansätze (see text). $\chi \to \infty$ linear extrapolations are performed using only the last data points. (b) Behavior of the $\chi \to \infty$ extrapolated energies vs the inverse of the bond dimension D. $D = 9$ PEPS [56] and DMRG [66] *extrapolated* energies are shown for comparison (see also Table II).

comparison between the different classes (for intermediate χ) reveals that for identical bond dimension D, the classes $V = \frac{1}{2}^{\otimes N} \oplus 0$ with $N = 1$, 2, and 3 (of bond dimensions $D = 3$, 5, and 7, respectively) give the best results. Hence, hereafter we shall focus on this PEPS family defined in terms of N "colors" of spin-$\frac{1}{2}$. Note that the case $N = 1$ was studied previously in Ref. [69]. Tensors are fully optimized up to a maximum bond dimension $\chi_{\rm opt}$, e.g., for $D = 5$, $\chi_{\rm opt} = 4D^2 = 100$ and, for $D = 7$, $\chi_{\rm opt} = 2D^2 = 98$. Then, using environment dimensions $\chi > \chi_{\rm opt}$ together with the fixed optimized tensor obtained at $\chi = \chi_{\rm opt}$, one gets the true *upper bounds* of the variational energy. In contrast, for $D = 3$, $\chi_{\rm opt} = 12D^2 = 108$ already gives the absolute best tensor with enough accuracy. Generically, we found that the energy always decreases with increasing χ and, at large enough χ, linear fits can be performed in $1/\chi$ to provide $\chi \to \infty$ extrapolations, also upper bounds of the (D-dependent) variational energies. Note that our $D = 7$ extrapolation -0.49502 lies within only 0.2% of the extrapolated value -0.4958 obtained using cluster update finite-size $D = 9$ PEPS [56]. We have plotted our ($\chi \to \infty$) results as a function of $1/D$ in Fig. 3(b), showing perfect consistency with the above-mentioned $D = 9$ result together with the DMRG extrapolation -0.4968 of Ref. [66]. This agreement is remarkable considering the fact that we use only a unique tensor parametrized by a small number of coefficients. Good variational energies have also been found for the simple NN Heisenberg model ($J_2 = 0$) as well as for larger frustration $J_2 = 0.55$, as shown in Appendix A. Our results are summarized in Table II and compared to the best estimates, from quantum Monte Carlo at $J_2 = 0$ [4,5] and from DMRG [66], VMC [70], and finite-size PEPS [56] at $J_2 = 0.5$ and $J_2 = 0.55$. We note, however, that our variational energies for $J_2 = 0$ and $J_2 = 0.55$ are slightly less accurate than for

TABLE II. Comparison between our $D = 7$ iPEPS results ($\chi \to \infty$ extrapolations) and the best estimates in the literature, for $J_2 = 0$, $J_2 = 0.5$, and $J_2 = 0.55$: $J_2 = 0$ results are obtained by QMC [4,5]. At finite J_2, we quote energies obtained by extrapolations to the thermodynamic limit using DMRG [66], VMC [70], and *finite-size* $D = 9$ PEPS [56]. Note that the $D = 7$ iPEPS energies are only upper bounds of the true variational energies (see text).

J	0	0.5	0.55
QMC	−0.66944		
DMRG		−0.4968	−0.4863
VMC		−0.4970(5)	−0.4870(5)
$D = 9$ PEPS		−0.4958(3)	−0.4857(2)
$D = 7$ iPEPS	−0.6677	−0.4950	−0.4830

$J_2 = 0.5$. In fact, we believe J_{2c} is close to 0.5 and we argue below that our (optimized) PEPS is capable of picking up the critical nature of the QCP or QCPh. For $J_2 = 0.55$, translation symmetry breaking is likely to occur spontaneously, which is not captured by our homogeneous ansatz. The ansatz also does not sustain magnetic LR order, which may explain its lower accuracy at $J_2 = 0$.

III. CORRELATION FUNCTIONS

Once the PEPS $|\Psi_0\rangle = |\Psi(D, \chi_{\rm opt})\rangle$ have been optimized using the largest possible environment dimension $\chi = \chi_{\rm opt}(D)$, various correlation functions can be computed (e.g., along the $\mathbf{e}_x$ horizontal direction), such as (i) the spin-spin correlations,

$$C_{\rm s}(d) = \langle \mathbf{S_i} \cdot \mathbf{S_{i+}}_{d\mathbf{e}_x} \rangle_0, \tag{1}$$

(ii) the (connected) *longitudinal* dimer-dimer correlations,

$$C_{\rm d}^{\rm (L)}(d) = \langle D_{\mathbf{i}}^x D_{\mathbf{i}+d\mathbf{e}_x}^x \rangle_0 - \langle D_{\mathbf{i}}^x \rangle_0 \langle D_{\mathbf{i}+d\mathbf{e}_x}^x \rangle_0, \tag{2}$$

and (iii) the (connected) *transverse* dimer-dimer correlations,

$$C_{\rm d}^{\rm (T)}(d) = \langle D_{\mathbf{i}}^y D_{\mathbf{i}+d\mathbf{e}_x}^y \rangle_0 - \langle D_{\mathbf{i}}^y \rangle_0 \langle D_{\mathbf{i}+d\mathbf{e}_x}^y \rangle_0, \tag{3}$$

where dimer operators $D_{\mathbf{i}}^x = \mathbf{S_i} \cdot \mathbf{S_{i+e}}_x$ and $D_{\mathbf{i}}^y = \mathbf{S_i} \cdot \mathbf{S_{i+e}}_y$ are oriented either along the $\mathbf{e}_x$ (horizontal) or $\mathbf{e}_y$ (vertical) directions, respectively, and the expectation values are taken in the optimized $|\Psi_0\rangle$ PEPS.

The calculations of correlators are accomplished using the setup shown in Figs. 4(a)–4(c). Appropriate transfer matrices are used so that one can construct arbitrarily long strips. Here the site tensor is fixed to its optimized output using $\chi = \chi_{\rm opt}(D)$ (hereafter we use $\chi_{\rm opt} = 49$ for $D = 7$), while the environment dimension $\chi > \chi_{\rm opt}(D)$ can then be further increased to reach convergence, which is easily achieved for short distance r. A comparison between the results obtained with the two Ansätze $V = \frac{1}{2} \oplus \frac{1}{2} \oplus 0$ [Fig. 5(a)] and $V = \frac{1}{2} \oplus \frac{1}{2} \oplus \frac{1}{2} \oplus 0$ [Fig. 5(b)] is shown for $J_2 = 0.5$. Although a fast decay of the dimer-dimer correlations is seen in both cases, the behavior of the (staggered) spin-spin correlations is qualitatively different: for $D = 7$, $|C_{\rm s}(r)|$ seems to approach a finite value, while for $D = 5$ (or $D = 3$ as well), it steadily decays to zero. This signals the emergence, for $D \geqslant 7$, of a finite staggered magnetization as defined by

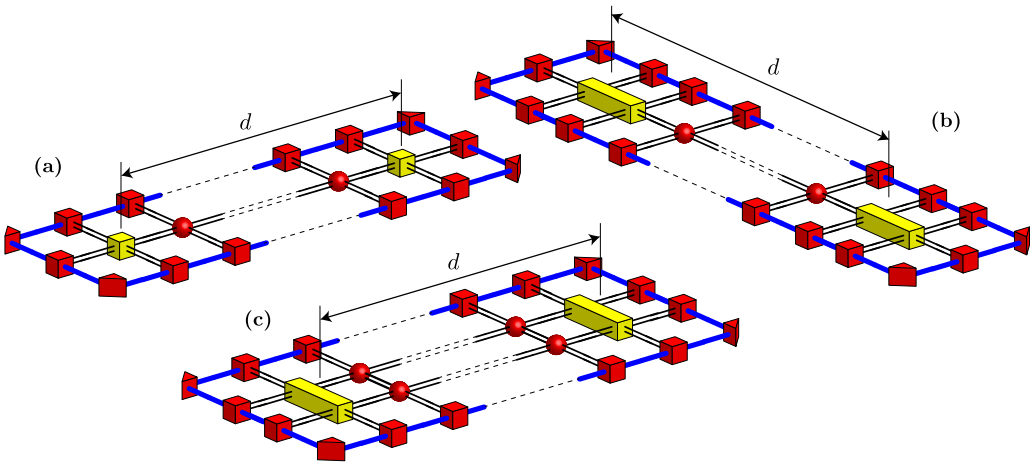

FIG. 4. One-dimensional strips used to compute (a) the spin-spin, (b) the longitudinal dimer-dimer, and (c) the transverse dimer-dimer correlation functions. A transfer matrix is applied recursively (a),(c) $d-1$ times or (b) $d-2$ times in the direction of the strip.

$m_{\rm stag}(\chi)=\sqrt{\lim_{r\to\infty}|C_{\rm s}(r)|}$. We note, however, that strictly speaking, for finite χ the above limit should vanish since the correlations are cut off above some correlation length $\xi_{\rm s}(\chi)$ (see below). In other words, the strip of Fig. 4(a) is, crudely speaking, similar to a quasi-1D physical strip (ladder) of effective width $L_{\rm eff}(\chi)$ [80], which cannot sustain long-range magnetic order from Mermin-Wagner theorem (MWT) [81]. However, MWT may not, strictly speaking, apply to a transfer operator as for a true Hamiltonian. In addition, for $D=7$, the SU(2) symmetry is spontaneously broken: small deviations from a perfectly SU(2)-symmetric environment act as a small symmetry-breaking (AF) "field" and the local spin operator acquires a finite value $\langle \mathbf{S_i}\rangle_0=\cos(\mathbf{q}_{\rm AF}\cdot\mathbf{i})\,\mathbf{m}_{\rm stag}$ oscillating at the antiferromagnetic wave vector $\mathbf{q}_{\rm AF}$. As shown in Appendix B, $m_{\rm stag}(\chi)$ vanishes in the $\chi\to\infty$ limit, physically corresponding to the limit of an infinitely wide strip $L_{\rm eff}\to\infty$. This implies that the infinite 2D system recovers the full SU(2) spin symmetry encoded in the tensor ansatz. We have seen similar behaviors for $J_2=0$ and $J_2=0.55$ as well (see Appendix B). Interestingly, the scaling of $m_{\rm stag}$ to zero may depend slightly on the initial CTM of the CTMRG procedure to converge the environment. In contrast, for $D=3$ and $D=5$, the system remains spin isotropic even for finite χ, the spin correlators $\langle S^\alpha_{\mathbf{i}} S^\alpha_{\mathbf{j}}\rangle_0$ being independent on $\alpha=x,y,z$, as checked explicitly. This signals a qualitative change of behavior when $N\geqslant 3$, which we identify in the next section.

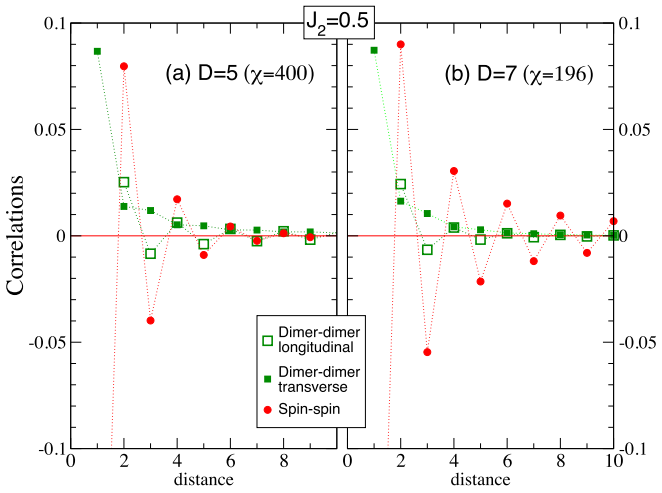

FIG. 5. Short-distance correlation functions at $J_2=0.5$ for (a) $V=\frac{1}{2}\oplus\frac{1}{2}\oplus 0$ and (b) $V=\frac{1}{2}\oplus\frac{1}{2}\oplus\frac{1}{2}\oplus 0$. Large environment dimensions χ are used ensuring full convergence of the correlations at short distance ($r<10$).

Diverging correlation lengths. The results described above give some hints that when $D=7$, the spin-spin correlations become algebraic at long distance. However, for finite bond dimension χ, the strips of Figs. 4(a)–4(c) can be seen as effective 1D systems. Then, finite correlation lengths $\xi_D(\chi)$ naturally emerge as the inverse of the gaps of *finite-dimensional* $D^2_{\rm eff}\times D^2_{\rm eff}$ transfer matrices, where $D_{\rm eff}=D\chi$ [Figs. 4(a) and 4(b)] or $D_{\rm eff}=D^2\chi$ [Fig. 4(c)] are the effective dimensions of the associated 1D MPS. Using empirical findings for the correlation length $\xi_{\rm 1D}$ in critical 1D systems [73–75], $\xi_{\rm 1D}(D)\sim D^\kappa$, one then expects that $\xi_D(\chi)\sim(D_{\rm eff})^\kappa$, $\kappa>0$, which should diverge with χ as a power law for critical PEPS. Hence, criticality (if any) is restored only in the $\chi\to\infty$ limit and finite-χ scaling is necessary to obtain information on the QCP or QCPh. Note that when spin-rotational symmetry is (artificially) broken at finite χ, it is important to consider the *connected* spin-spin correlator $\tilde{C}_{\rm s}(d)=C_{\rm s}(d)-(m_{\rm stag})^2$. From straightforward fits of the long-distance correlations at $J_2=0.5$ (see Appendix C), we have extracted the correlation lengths $\xi_D(\chi)$ associated to the $\tilde{C}_{\rm s}$, $C^{\rm (T)}_{\rm d}$, and $C^{\rm (L)}_{\rm d}$ correlation functions and results are shown in Fig. 6. For $D=3$ or $D=5$, we find a clear saturation of the spin-spin correlation lengths to small values, while the dimer-dimer correlations lengths diverge *linearly* with χ. Such a behavior is typical of bipartite dimer models [82] or of the NN RVB state on the square lattice [17,19] due to U(1)-gauge symmetry. In fact, the $D=3$ PEPS can be viewed as an extended-range RVB state [69] and the $D=5$ PEPS as an extended-range *two-color* RVB state. Plotting the dimer correlation lengths in Figs. 6(c) and 6(e) as a function of χ/D^2 clearly reveals the similarities between $D=5$ and $D=7$. However, in the case of the spin correlations, a sudden qualitative change occurs at $D=7$ for which we find that the spin-spin correlation length no longer saturates but increases linearly with χ, as the dimer correlation

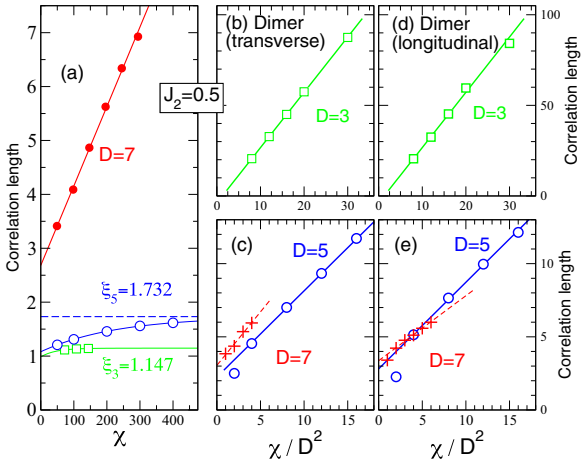

FIG. 6. Scaling of the various correlation lengths at $J_2 = 0.5$ vs (a) environment dimension χ or (b)–(e) χ/D^2, for $V = \frac{1}{2} \oplus 0$ (open squares), $V = \frac{1}{2} \oplus \frac{1}{2} \oplus 0$ (open circles), and $V = \frac{1}{2} \oplus \frac{1}{2} \oplus \frac{1}{2} \oplus 0$ (large dots and crosses). (a) Spin-spin correlations. (b),(c) Transverse dimer-dimer correlations. (d),(e) Longitudinal dimer-dimer correlations.

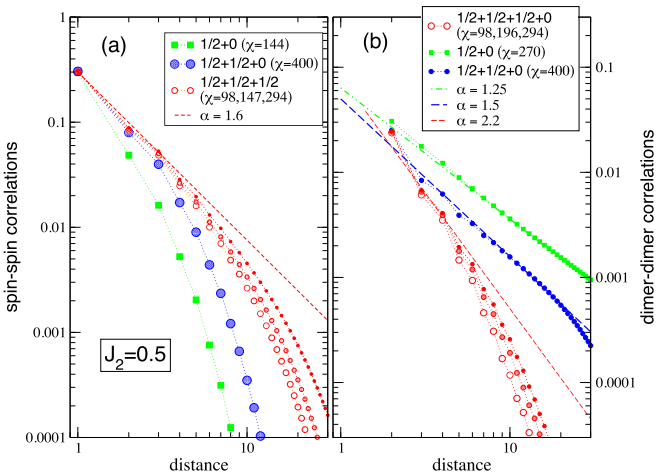

FIG. 7. (a) Log-log plot of (a) spin-spin and (b) longitudinal dimer-dimer correlations vs distance. Straight (dashed) lines correspond to power-law decays $\sim d^{-\alpha}$.

lengths do (see Appendices C and D for details). No sign of saturation of the correlation lengths is observed up to the largest available environment dimensions. This suggests that the (optimized) $D = 7$ PEPS is critical in the limit $\chi \to \infty$ or, at least, can very well describe a critical state.

Power-law exponents. Whenever the correlation length $\xi_D(\chi)$ diverges (or becomes very large), one expects to see power-law behaviors in the correlation functions,

$$C_s(d) \sim d^{-(1+\eta_s)}, \tag{4}$$

$$C_d(d) \sim d^{-(1+\eta_d)}, \tag{5}$$

in the range of distance $1 < d < \xi_D$, where η_s and η_d defined, e.g., in Ref. [83] are the anomalous dimensions. Note, however, that this scaling regime can be observed only when $\xi_D(\chi)$ has reached a sufficiently large value. To obtain estimates of the exponents $1 + \eta_s$ and $1 + \eta_d$, we have plotted spin-spin and (longitudinal) dimer-dimer correlations at $J_2 = 0.5$ in Figs. 7(a) and 7(b) using log-log scales. For $D = 3$ ($D = 5$), the dimer correlation length is very large (is large) for the largest χ we can reach and, from fits of the data in the range $1 < d < 100$ ($1 < d < 20$), one can easily extract the exponent $1 + \eta_d \simeq 1.25$ ($1 + \eta_d \simeq 1.5$). For $D = 7$, it is difficult to extract accurate exponents since crossovers to exponential decays occur rapidly around $d \sim \xi_7 \simeq 6$, for both the spin-spin and dimer-dimer correlations. However, the systematic trend of the data with χ in Figs. 7(a) and 7(b) suggests $\eta_s \sim 0.6$ and $\eta_d \sim 1.2$.

Discussion and outlook. Above, we have found solid evidence that the $N = 3$ ($D = 7$) SU(2)-invariant state exhibits slowly (possibly power-law) decaying spin-spin and dimer-dimer correlation functions, suggesting a critical behavior or at least very large correlation lengths. We now argue that the family of SU(2)-symmetric tensors characterized by the virtual space $V = \frac{1}{2}^{\otimes N} \oplus 0$ with $N \geqslant 3$ "colors" can faithfully describe the QCP or QCPh of the spin-$\frac{1}{2}$ $J_1 - J_2$ Heisenberg model.

First, we observed that spin-spin correlations decay less and less rapidly for increasing N (i.e., D) so we expect such correlations to become longer and longer range for increasing N. Since the anomalous dimension η_s (defined from the correlation at intermediate distances) generically decreases with increasing D, one can put an upper bound to its infinite-D limit, namely, $\eta_s < 0.6$.

Second, it is remarkable that dimer-dimer correlations (and correlation lengths) become very similar for $N = 2$ and $N = 3$, if compared at the same value of the ratio χ/D^2. In fact, we may speculate that for $N \geqslant 3$, all correlation lengths diverge as

$$\xi_D(\chi) \simeq f_D\, \chi/D^2, \tag{6}$$

where the prefactor f_D depends weakly on D, the main effect of increasing the bond dimension being to rescale the environment dimension $\chi \to \chi_D = \chi/D^2$. We note, nevertheless, that although our data are consistent with (6), one cannot rule out that some of the correlation lengths may saturate to a finite, although large, value.

Related $J - Q$ models can be investigated with QMC [83] and $\eta_s \simeq 0.35(2)$ and $\eta_d \simeq 0.20(2)$ have been obtained (for the $J - Q_2$ model), which seem to deviate substantially from our estimates above. However, our estimation of η_s seems consistent with the VMC result [71] $\eta_s \sim 0.5$ obtained for the $J_1 - J_2$ Heisenberg model at $J_2 = 0.5$.

Note that the power-law exponent $1 + \eta_d$, extracted from the correlations at intermediate distances $d < \xi_D(\chi)$, seems to increase significantly with D. The predicted large value of the $D \to \infty$ dimer anomalous dimension might indicate that dimer correlations at the QCP or within the QCPh are significantly suppressed compared to $J - Q$ models.

ACKNOWLEDGMENTS

This project is supported by the TNSTRONG ANR grant (French Research Council). This work was granted access to the HPC resources of CALMIP supercomputing center under the allocations 2016-P1231 and 2017-P1231. D.P. thanks

Nicolas Renon (CALMIP) and Cyril Mazauric (ATOS) for assistance. D.P. acknowledges illuminating discussions with Philippe Corboz, as well as helpful advice to implement the CTM algorithm. M.M. and D.P. thank Roman Orus for insightful comments. D.P. also acknowledges inspiring conversations with Fabien Alet, Federico Becca, Ignacio Cirac, Shenghan Jiang, Naoki Kawashima, Frédéric Mila, David Perez-Garcia, Frank Pollmann, Pierre Pujol, Ying Ran, Anders Sandvik, Norbert Schuch, Frank Verstraete, and Ling Wang.

APPENDIX A: SCALING OF THE $D = 7$ VARIATIONAL ENERGY VS INVERSE ENVIRONMENT DIMENSION

We report in Figs. 8(a)–8(c) the variational energies of the $V = \frac{1}{2} \oplus \frac{1}{2} \oplus \frac{1}{2} \oplus 0$ PEPS ansatz for the $J_1 - J_2$ model at $J_2 = 0$ (unfrustrated case), $J_2 = 0.5$, and $J_2 = 0.55$. The parameters of the PEPS are optimized with an environment dimension $\chi_{\text{opt}} = D^2 = 49$, independently for each value of J_2. For $J_2 = 0.5$, we also carried out the optimization with $\chi_{\text{opt}} = 2D^2 = 98$, providing a slightly better energy. The environment dimension $\chi > \chi_{\text{opt}}$ is then increased, keeping the PEPS tensor fixed, and the energy is extrapolated linearly with $1/\chi$. At $J_2 = 0.5$, an excellent agreement is found with extrapolation from $D = 9$ PEPS cluster update [56]. For $J_2 = 0$ and $J_2 = 0.55$, a lesser agreement is found with QMC [4,5] and $D = 9$ PEPS cluster update [56], respectively (see text for explanation).

APPENDIX B: SCALING OF THE $D = 7$ STAGGERED MAGNETIZATION VS INVERSE ENVIRONMENT DIMENSION

We report in Figs. 9(a)–9(c) the spurious staggered magnetization of the $V = \frac{1}{2} \oplus \frac{1}{2} \oplus \frac{1}{2} \oplus 0$ PEPS ansatz for the $J_1 - J_2$ model at $J_2 = 0$ (unfrustrated case), $J_2 = 0.5$, and $J_2 = 0.55$ (optimized using $\chi_{\text{opt}} = D^2 = 49$). The procedure is the same as in Appendix A and the data are plotted vs χ. For all J_2 values, the scaling (algebraic fits) is consistent with vanishing m_{stag} when $\chi \to \infty$. Full SU(2) invariance is recovered in this case.

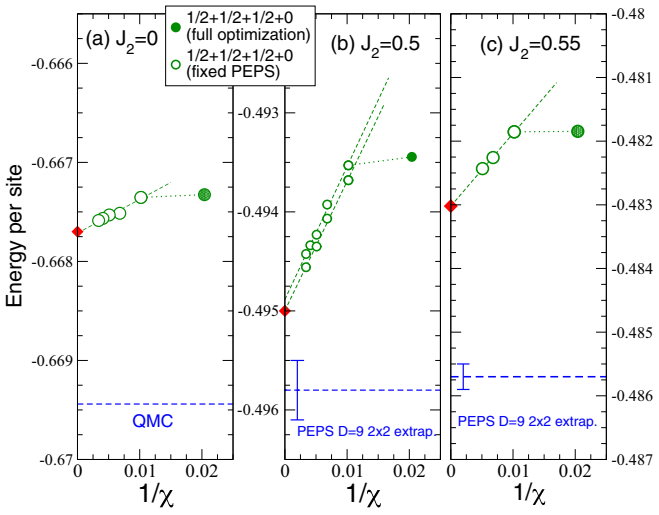

FIG. 8. (a) $D = 7$ iPEPS variational energies of the $J_1 - J_2$ model at (a) $J_2 = 0$, (b) $J_2 = 0.5$, and (c) $J_2 = 0.55$ vs the inverse of the environment dimension χ. Full (open) symbols correspond to fully optimized (fixed) tensor Ansätze (see text). $\chi \to \infty$ linear extrapolations are performed using only the last data points. Comparisons with QMC [4,5] and *finite-size* $D = 9$ PEPS extrapolations (with error bars) [56] are shown.

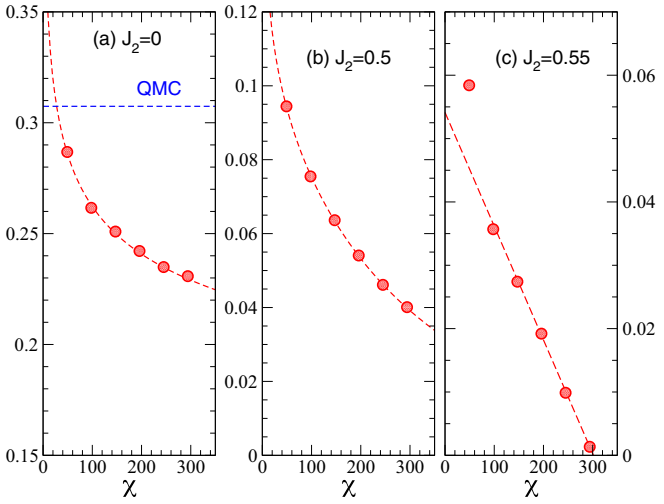

FIG. 9. (a) $D = 7$ iPEPS staggered magnetization of the $J_1 - J_2$ model at (a) $J_2 = 0$, (b) $J_2 = 0.5$, and (c) $J_2 = 0.55$ vs environment dimension χ. $\chi \to \infty$ extrapolations are based on power-law fits. The exact (QMC) value of m_{stag} [4,5] at $J_2 = 0$ is shown.

APPENDIX C: EXTRACTING THE CORRELATION LENGTHS $\xi_D(\chi)$ FROM THE LONG-DISTANCE CORRELATIONS

In order to extract the correlation lengths associated to the various correlation functions $C_\lambda(d)$ ($\lambda = S, D$) defined in the paper in Eqs. (1)–(3), we have computed the long-distance correlations using the transfer matrix methods sketched in Fig. 2. Due to a finite gap in the relevant transfer matrices for all finite dimensions D and χ, one expects an exponential decay of all correlations,

$$C_\lambda(d) \sim C_0 \exp\left[-d/\xi_D(\chi)\right],$$

at sufficiently large distance d [typically $d > \xi_D(\chi)$]. Let us summarize the procedure: First, the local tensors for $D = 3$, 5, and 7 are obtained by a full CG optimization (for $J_2 = 0.5$) using a given environment dimension $\chi_{\text{opt}} = 108$, 100, and 49, respectively. The correlations in these fixed PEPS are then computed for increasing values of the environment dimension χ in two steps: (i) For every choice of $\chi \geqslant \chi_{\text{opt}}$, the new converged CTM C and edge tensor T are computed (by the iterative renormalization scheme) and, finally, (ii) used to compute the correlation functions in the setup shown in Figs. 2(a)–2(c). Results are displayed using semilogarithmic scales in Figs. 10(a), 11(a), and 12(a). By fitting the asymptotic linear behaviors of the data according to $\ln C_\lambda(d) = -(1/\xi)d + c_0$, one straightforwardly gets the correlation lengths ξ from the slopes $-1/\xi$.

The scaling of the correlation lengths ξ_D with χ is shown in Figs. 10(b), 11(b), 11(c), 12(b), and 12(c). For $D = 3$ and $D = 5$, one observes a clear saturation of the spin correlation lengths ξ_3 and ξ_5 to rather small values (less than two lattice spacings),

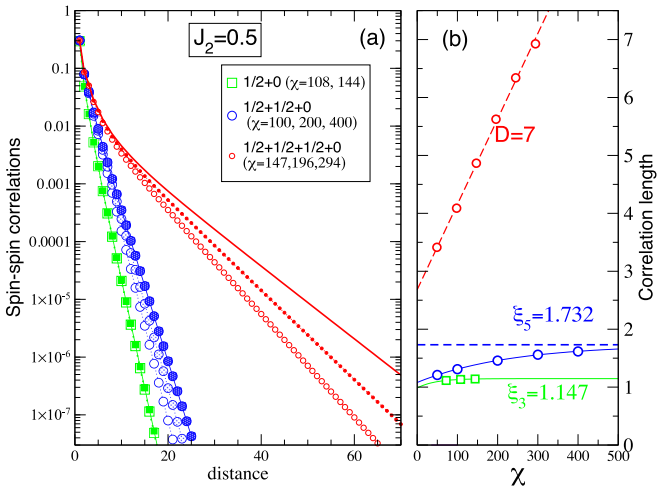

FIG. 10. (a) Spin-spin correlation vs distance for (fixed) $D = 3$, $D = 5$, and $D = 7$ tensors and several dimension χ of the environment (semilogarithmic scale). The tensors are obtained from a full CG optimization using environment dimensions $\chi_{\rm opt} = 108$, 100, and 49, respectively. (b) Correlation length extracted from linear fits of the asymptotic large-distance behaviors are shown vs χ.

while the dimer correlation length scales linearly with χ, suggesting that $\xi_D \to \infty$ in the limit $\chi \to \infty$, for which the calculation becomes exact. Note that the (extrapolated) spin correlation length increases with D, while the divergence of the dimer correlation length becomes weaker. For $D = 7$, one has to consider the *connected* part of the spin-spin correlation, subtracting the contribution from the spurious staggered spin-density background. The spin correlation length no longer saturates but rather increases linearly with the environment dimension χ. This strongly suggests that ξ_7 diverges in the limit $\chi \to \infty$, which is consistent with a power-law decay of the correlation function. We believe our numerical results also support the divergence of both dimer-dimer correlation

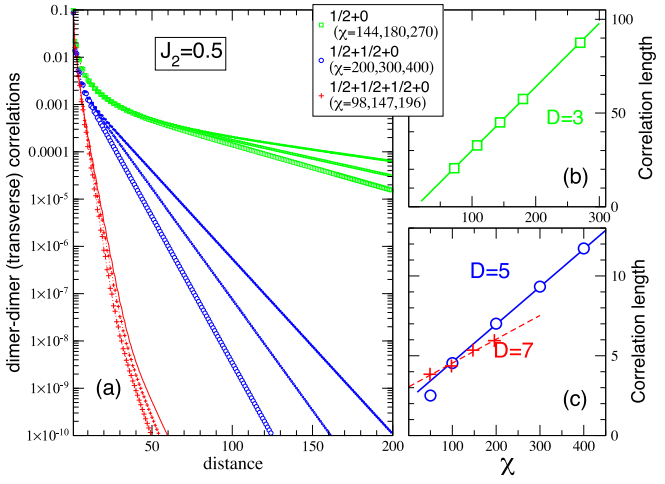

FIG. 11. (a) Transverse dimer-dimer correlation vs distance for $D = 3$, $D = 5$, and $D = 7$ and several values of χ (semilogarithmic scale). Tensors are the same as in Fig. 10. (b),(c) Correlation lengths extracted from linear fits of the asymptotic large-distance behaviors are shown vs χ.

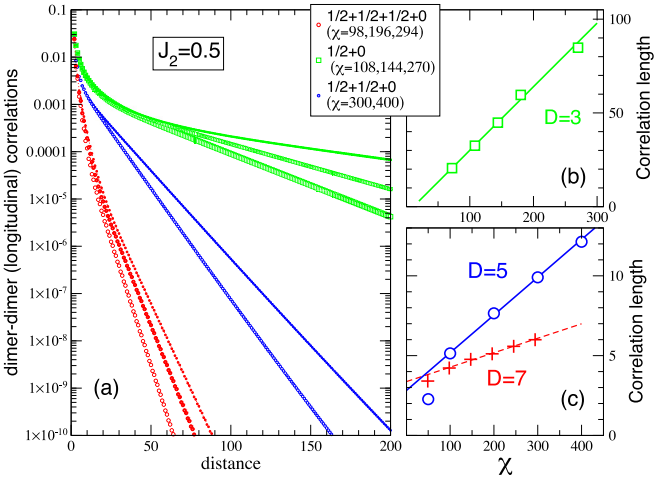

FIG. 12. (a) Longitudinal dimer-dimer correlation vs distance for $D = 3$, $D = 5$, and $D = 7$ and several values of χ (semilogarithmic scale). Tensors are the same as in Fig. 10. (b),(c) Correlation lengths extracted from linear fits of the asymptotic large-distance behaviors are shown vs χ.

lengths. Note, however, that although the transverse and longitudinal dimer-dimer correlation lengths seem to match for $D = 3$ and $D = 5$, they deviate substantially for $D = 7$, which may be related to the nonvanishing of the spin-spin correlation in that case.

APPENDIX D: COMPARISON BETWEEN CORRELATION FUNCTIONS IN THE $D = 7$ PEPS

In principle, correlation lengths can also be extracted directly from the low-energy eigenvalues of the zero-dimensional transfer matrix of the one-dimensional tensor network structures arising in Fig. 4. It would be the same transfer matrix for the spin-spin and (longitudinal) dimer-dimer correlation function, but the difference would be how the corresponding virtual eigenvectors of these eigenvalues transform under the symmetry. In a perfectly SU(2)-symmetric state giving rise to a SU(2)-symmetric environment (as occurs for $D = 3$ and $D = 5$), different selection rules for the singlet (dimer) and the triplet (spin) channels lead to separate blocks of the transfer matrix and, hence, to different correlation lengths, in agreement with our findings. However, for $D = 7$, spontaneous SU(2) symmetry breaking occurs and the environment acquires some (staggered) magnetization $\mathbf{m}_{\rm stag}$. We believe spin-rotational invariance [U(1) symmetry] is still preserved around the direction of the staggered magnetization. The latter can be pointing in any (arbitrary) direction in the (x,z) plane, making difficult the symmetry analysis of the zero-dimensional transfer matrix arising in Fig. 4. Analysis of the correlation functions given, e.g., by Eqs. (1), (2), or (3) is more straightforward.

At this point, it is not clear whether the long-distance spin correlation described in the text is an artifact of the symmetry breaking that (i) may lead to a mixture of (diverging) singlet and (short-range) triplet correlations or (ii) may lead to "Goldstone critical behavior" of the transverse spin correlation function. We give arguments below that none of the above

applies and argue that the critical behavior of the spin correlation function is an intrinsic feature of the $D = 7$ PEPS spin liquid.

For this purpose, we decompose the local spin operator into its longitudinal and transverse spin components,

$$\mathbf{S_i} = S_\mathbf{i}^{\parallel}\,\mathbf{n} + \mathbf{S}_\mathbf{i}^{\perp}, \tag{D1}$$

where $\mathbf{n}$ is a unit vector along $\mathbf{m}_{\text{stag}}$, $S_\mathbf{i}^{\parallel} = \mathbf{S_i}\cdot\mathbf{n}$, and $\mathbf{S}_\mathbf{i}^{\perp} = \mathbf{S_i} - (\mathbf{S_i}\cdot\mathbf{n})\,\mathbf{n}$. The spin correlation function can then be split into its longitudinal and transverse components as $C_s(d) = C_s^{\parallel}(d) + C_s^{\perp}(d)$, with

$$C_s^{\parallel}(d) = \langle \mathbf{S_i}^{\parallel}\cdot\mathbf{S}^{\parallel}_{\mathbf{i}+d\mathbf{e}_x}\rangle_0, \tag{D2}$$

$$C_s^{\perp}(d) = \langle \mathbf{S_i}^{\perp}\cdot\mathbf{S}^{\perp}_{\mathbf{i}+d\mathbf{e}_x}\rangle_0. \tag{D3}$$

For a true singlet wave function (for which $\mathbf{m}_{\text{stag}} = \mathbf{0}$), whatever the choice of the vector $\mathbf{n}$, one gets $C_s^{\perp}(d) = 2C_s^{\parallel}(d)$. As shown in Fig. 13(a), this is also true for the $D = 7$ PEPS, at *short distance* only (in semilogarithmic scale, the two curves are just shifted by $\ln 2$). At longer distance, however, the longitudinal and transverse spin correlations show different exponential decays. As shown in Fig. 13(b), the correlation length of the longitudinal correlations is much shorter than the one of the transverse correlations. However, both seem to diverge with increasing χ, suggesting that both correlators are critical, possibly power law, in the $\chi \to \infty$ limit. This is different from a "Goldstone mechanism" for which the longitudinal correlations remain short range. Finally, we compare the two spin correlation lengths to the (longitudinal) dimer correlation length. Figure 13(b) shows that none of the three (diverging) correlation lengths match, suggesting that the (supposedly) critical behavior of the spin-spin correlation is not induced by the critical behavior of the dimer correlation and is an intrinsic property of the $D = 7$ PEPS.

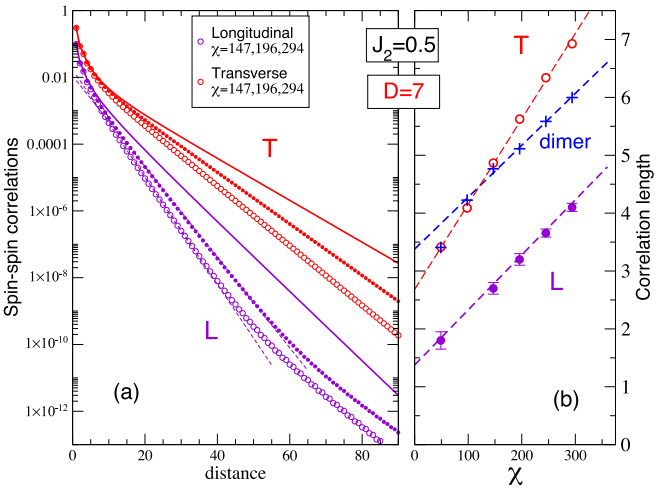

FIG. 13. (a) Longitudinal and transverse spin correlations vs distance in the SU(2) symmetry broken $D = 7$ PEPS, for several values of χ (semilogarithmic scale). Tensors are the same as in Fig. 10. (b) Correlation lengths extracted from linear fits of the large-distance behaviors are shown vs χ and compared to the (longitudinal) dimer correlations. Note that, eventually, beyond some large crossover length scale (which increases with χ), the decay of the longitudinal correlation function is governed by the asymptotic (larger) correlation length of the transverse correlation function.

[1] T. Senthil, A. Vishwanath, L. Balents, S. Sachdev, and M. P. A. Fisher, Deconfined quantum critical points, Science **303**, 1490 (2004).

[2] H. Shao, W. Guo, and A. W. Sandvik, Quantum criticality with two length scales, Science **352**, 213 (2016).

[3] J. D. Reger and A. P. Young, Monte carlo simulations of the spin-1/2 Heisenberg antiferromagnet on a square lattice, Phys. Rev. B **37**, 5978(R) (1988).

[4] A. W. Sandvik and H. G. Evertz, Loop updates for variational and projector quantum monte carlo simulations in the valence-bond basis, Phys. Rev. B **82**, 024407 (2010).

[5] A. W. Sandvik, Computational studies of quantum spin systems, in *XIV Training Course in the Physics of Strongly Correlated Systems, Salerno (Vietri sul Mare), Italy, 2009*, Vol. 1297, edited by A. Avella and F. Mancini (American Institute of Physics, Melville, New York, 2010), p. 135.

[6] P. Chandra and B. Douçot, Possible spin-liquid state at large S for the frustrated square Heisenberg lattice, Phys. Rev. B **38**, 9335(R) (1988).

[7] E. Dagotto and A. Moreo, Exact diagonalization study of the frustrated Heisenberg model: A new disordered phase, Phys. Rev. B **39**, 4744(R) (1989).

[8] S. Sachdev and N. Read, Large N expansion for frustrated and doped quantum antiferromagnets, Int. J. Mod. Phys. B **05**, 219 (1991).

[9] F. Mila, D. Poilblanc, and C. Bruder, Spin dynamics in a frustrated magnet with short-range order, Phys. Rev. B **43**, 7891 (1991).

[10] N. Read and S. Sachdev, Valence-Bond and Spin-Peierls Ground States of Low-Dimensional Quantum Antiferromagnets, Phys. Rev. Lett. **62**, 1694 (1989).

[11] E. Dagotto and A. Moreo, Phase Diagram of the Frustrated Spin-1/2 Heisenberg Antiferromagnet in 2 Dimensions, Phys. Rev. Lett. **63**, 2148 (1989).

[12] D. Poilblanc, E. Gagliano, S. Bacci, and E. Dagotto, Static and dynamical correlations in a spin-1/2 frustrated antiferromagnet, Phys. Rev. B **43**, 10970 (1991).

[13] H. J. Schulz, T. A. L. Ziman, and D. Poilblanc, Magnetic order and disorder in the frustrated quantum heisenberg antiferromagnet in two dimensions, J. Phys. I France **6**, 675 (1996).

[14] M. E. Zhitomirsky and K. Ueda, Valence-bond crystal phase of a frustrated spin-1/2 square-lattice antiferromagnet, Phys. Rev. B **54**, 9007 (1996).

[15] M. Mambrini, A. Läuchli, D. Poilblanc, and F. Mila, Plaquette valence-bond crystal in the frustrated Heisenberg quantum antiferromagnet on the square lattice, Phys. Rev. B **74**, 144422 (2006).

[16] P. W. Anderson, Resonating valence bonds: A new kind of insulator? Mater. Res. Bull. **8**, 153 (1973).

[17] A. F. Albuquerque and F. Alet, Critical correlations for short-range valence-bond wave functions on the square lattice, Phys. Rev. B **82**, 180408(R) (2010).

[18] Y. Tang, A. W. Sandvik, and C. L. Henley, Properties of resonating-valence-bond spin liquids and critical dimer models, Phys. Rev. B **84**, 174427 (2011).

[19] D. Poilblanc, N. Schuch, D. Pérez-García, and J. I. Cirac, Topological and entanglement properties of resonating valence bond wave functions, Phys. Rev. B **86**, 014404 (2012).

[20] N. Schuch, D. Poilblanc, J. I. Cirac, and D. Pérez-García, Resonating valence bond states in the PEPS formalism, Phys. Rev. B **86**, 115108 (2012).

[21] L. Wang and A. Sandvik, Critical level crossings and gapless spin liquid in the square-lattice spin-1/2 $J_1 - J_2$ Heisenberg antiferromagnet, arXiv:1702.08197.

[22] J. I. Cirac and F. Verstraete, Renormalization and tensor product states in spin chains and lattices, J. Phys. A: Math. Theor. **42**, 504004 (2009).

[23] J. I. Cirac, Entanglement in many-body quantum systems, in *Many-Body Physics with Ultracold Gases: Lecture Notes of the Les Houches Summer School*, edited by C. Salomon, G. V. Shlyapnikov, and L. F. Cugliandolo, Vol. 94 (Oxford University Press, Oxford, 2012).

[24] R. Orús, A practical introduction to tensor networks: Matrix product states and projected entangled pair states, Ann. Phys. **349**, 117 (2014).

[25] N. Schuch, Condensed matter applications of entanglement theory, *Quantum Information Processing: Lecture Notes*, Schriften des Forschungszentrums Jülich. Reihe Schlüsseltechnologien/Key Technologies, 44th IFF Spring School (David P. DiVincenzo, Forschungszentrum Jülich, 2013), p. 29.

[26] R. Orús, Advances on tensor network theory: Symmetries, fermions, entanglement, and holography, Eur. Phys. J. B **87**, 1 (2014).

[27] S. R. White, Density Matrix Formulation for Quantum Renormalization Groups, Phys. Rev. Lett. **69**, 2863 (1992).

[28] D. Pérez-García, F. Verstraete, J. I. Cirac, and M. M. Wolf, PEPS as unique ground states of local Hamiltonians, Quantum Inf. Comp. **8**, 0650 (2008).

[29] M. Mambrini, R. Orús, and D. Poilblanc, Systematic construction of spin liquids on the square lattice from tensor networks with SU(2) symmetry, Phys. Rev. B **94**, 205124 (2016).

[30] D. Pérez-García, M. Sanz, C. E. González-Guillén, M. M. Wolf, and J. I. Cirac, Characterizing symmetries in a projected entangled pair state, New J. Phys. **12**, 025010 (2010).

[31] N. Schuch, J. I. Cirac, and D. Pérez-García, PEPS as ground states: Degeneracy and topology, Ann. Phys. **325**, 2153 (2010).

[32] S. Singh, R. N. C. Pfeifer, and G. Vidal, Tensor network decompositions in the presence of a global symmetry, Phys. Rev. A **82**, 050301 (2010).

[33] S. Singh and G. Vidal, Tensor network states and algorithms in the presence of a global SU(2) symmetry, Phys. Rev. B **86**, 195114 (2012).

[34] S. Singh and G. Vidal, Global symmetries in tensor network states: Symmetric tensors versus minimal bond dimension, Phys. Rev. B **88**, 115147 (2013).

[35] A. Weichselbaum, Non-Abelian symmetries in tensor networks: A quantum symmetry space approach, Ann. Phys. **327**, 2972 (2012).

[36] S. Jiang and Y. Ran, Symmetric tensor networks and practical simulation algorithms to sharply identify classes of quantum phases distinguishable by short-range physics, Phys. Rev. B **92**, 104414 (2015).

[37] J. Haegeman, K. V. Acoleyen, N. Schuch, J. I. Cirac, and F. Verstraete, Gauging Quantum States: From Global to Local Symmetries in Many-Body Systems, Phys. Rev. X **5**, 011024 (2015).

[38] J. I. Cirac, D. Poilblanc, N. Schuch, and F. Verstraete, Entanglement spectrum and boundary theories with projected entangled-pair states, Phys. Rev. B **83**, 245134 (2011).

[39] S. Yang, L. Lehman, D. Poilblanc, K. Van Acoleyen, F. Verstraete, J. I. Cirac, and N. Schuch, Edge Theories in Projected Entangled Pair State Models, Phys. Rev. Lett. **112**, 036402 (2014).

[40] C.-M. Jian and M. Zaletel, Existence of featureless paramagnets on the square and the honeycomb lattices in 2+1 dimensions, Phys. Rev. B **93**, 035114 (2016).

[41] D. Poilblanc and N. Schuch, Simplex $\mathbb{Z}_2$ spin liquids on the kagome lattice with projected entangled pair states: Spinon and vison coherence lengths, topological entropy, and gapless edge modes, Phys. Rev. B **87**, 140407 (2013).

[42] W. Li, S. Yang, M. Cheng, Z.-X. Liu, and H.-H. Tu, Topology and criticality in the resonating Affleck-Kennedy-Lieb-Tasaki loop spin liquid states, Phys. Rev. B **89**, 174411 (2014).

[43] D. Poilblanc, N. Schuch, and J. I. Cirac, Field-induced superfluids and Bose liquids in projected entangled pair states, Phys. Rev. B **88**, 144414 (2013).

[44] D. Poilblanc, P. Corboz, N. Schuch, and J. I. Cirac, Resonating-valence-bond superconductors with fermionic projected entangled pair states, Phys. Rev. B **89**, 241106 (2014).

[45] J. Haegeman and F. Verstraete, Diagonalizing transfer matrices and matrix product operators: A medley of exact and computational methods, Annu. Rev. Condens. Matter Phys. **8**, 355 (2017).

[46] J. Jordan, R. Orús, G. Vidal, F. Verstraete, and J. I. Cirac, Classical Simulation of Infinite-Size Quantum Lattice Systems in Two Spatial Dimensions, Phys. Rev. Lett. **101**, 250602 (2008).

[47] T. Nishino and K. Okunishi, Corner transfer matrix renormalization group method, J. Phys. Soc. Jpn. **65**, 891 (1996).

[48] T. Nishino, Y. Hieida, K. Okunishi, N. Maeshima, Y. Akutsu, and A. Gendiar, Two-dimensional tensor product variational formulation, Prog. Theor. Phys. **105**, 409 (2001).

[49] R. Orús and G. Vidal, Simulation of two-dimensional quantum systems on an infinite lattice revisited: Corner transfer matrix for tensor contraction, Phys. Rev. B **80**, 094403 (2009).

[50] R. Orús, Exploring corner transfer matrices and corner tensors for the classical simulation of quantum lattice systems, Phys. Rev. B **85**, 205117 (2012).

[51] G. Vidal, Classical Simulation of Infinite-Size Quantum Lattice Systems in One Spatial Dimension, Phys. Rev. Lett. **98**, 070201 (2007).

[52] R. Orús and G. Vidal, Infinite time-evolving block decimation algorithm beyond unitary evolution, Phys. Rev. B **78**, 155117 (2008).

[53] G. Vidal, Efficient Classical Simulation of Slightly Entangled Quantum Computations, Phys. Rev. Lett. **91**, 147902 (2003).

[54] H. C. Jiang, Z. Y. Weng, and T. Xiang, Accurate Determination of Tensor Network State of Quantum Lattice Models in Two Dimensions, Phys. Rev. Lett. **101**, 090603 (2008).

[55] H. N. Phien, J. A. Bengua, H. D. Tuan, P. Corboz, and R. Orús, Infinite projected entangled pair states algorithm improved: Fast full update and gauge fixing, Phys. Rev. B **92**, 035142 (2015).

[56] L. Wang, Z.-C. Gu, F. Verstraete, and X.-G. Wen, Tensor-product state approach to spin-$\frac{1}{2}$ square J_1-J_2 antiferromagnetic Heisenberg model: Evidence for deconfined quantum criticality, Phys. Rev. B **94**, 075143 (2016).

[57] P. Corboz, Variational optimization with infinite projected entangled-pair states, Phys. Rev. B **94**, 035133 (2016).

[58] L. Vanderstraeten, J. Haegeman, P. Corboz, and F. Verstraete, Gradient methods for variational optimization of projected entangled-pair states, Phys. Rev. B **94**, 155123 (2016).

[59] W.-Y. Liu, S.-J. Dong, Y.-J. Han, G.-C. Guo, and L. He, Gradient optimization of finite projected entangled pair states, Phys. Rev. B **95**, 195154 (2017).

[60] A. B. Kallin, M. B. Hastings, R. G. Melko, and R. R. P. Singh, Anomalies in the entanglement properties of the square-lattice Heisenberg model, Phys. Rev. B **84**, 165134 (2011).

[61] M. A. Metlitski and T. Grover, Entanglement entropy of systems with spontaneously broken continuous symmetry, arXiv:1112.5166.

[62] H. Ju, A. B. Kallin, P. Fendley, M. B. Hastings, and R. G. Melko, Entanglement scaling in two-dimensional gapless systems, Phys. Rev. B **85**, 165121 (2012).

[63] D. Poilblanc, Entanglement Hamiltonian of the quantum Nel state, J. Stat. Mech.: Theor. Expt. (2014) P10026.

[64] M. Lubasch, J. I. Cirac, and M.-C. Bañuls, Algorithms for finite projected entangled pair states, Phys. Rev. B **90**, 064425 (2014).

[65] L. Capriotti and S. Sorella, Spontaneous Plaquette Dimerization in the J_1-J_2 Heisenberg Model, Phys. Rev. Lett. **84**, 3173 (2000).

[66] S.-S. Gong, W. Zhu, D. N. Sheng, O. I. Motrunich, and M. P. A. Fisher, Plaquette Ordered Phase and Quantum Phase Diagram in the Spin-$\frac{1}{2}$ J_1-J_2 Square Heisenberg Model, Phys. Rev. Lett. **113**, 027201 (2014).

[67] H.-C. Jiang, H. Yao, and L. Balents, Spin liquid ground state of the spin-$\frac{1}{2}$ square J_1-J_2 Heisenberg model, Phys. Rev. B **86**, 024424 (2012).

[68] L. Capriotti, F. Becca, A. Parola, and S. Sorella, Resonating Valence Bond Wave Functions for Strongly Frustrated Spin Systems, Phys. Rev. Lett. **87**, 097201 (2001).

[69] L. Wang, D. Poilblanc, Z.-C. Gu, X.-G. Wen, and F. Verstraete, Constructing a Gapless Spin-Liquid State for the Spin-1/2 J_1-J_2 Heisenberg Model on a Square Lattice, Phys. Rev. Lett. **111**, 037202 (2013).

[70] W.-J. Hu, F. Becca, A. Parola, and S. Sorella, Direct evidence for a gapless Z_2 spin liquid by frustrating Néel antiferromagnetism, Phys. Rev. B **88**, 060402 (2013).

[71] S. Morita, R. Kaneko, and M. Imada, Quantum spin liquid in spin 1/2 J_1-J_2Heisenberg model on square lattice: Many-variable variational Monte Carlo study combined with quantum-number projections, J. Phys. Soc. Jpn. **84**, 024720 (2015).

[72] R. Kaneko, L. F. Tocchio, R. Valentí, F. Becca, and C. Gros, Spontaneous symmetry breaking in correlated wave functions, Phys. Rev. B **93**, 125127 (2016).

[73] L. Tagliacozzo, T. R. de Oliveira, S. Iblisdir, and J. I. Latorre, Scaling of entanglement support for matrix product states, Phys. Rev. B **78**, 024410 (2008).

[74] F. Pollmann, S. Mukerjee, A. M. Turner, and J. E. Moore, Theory of Finite-Entanglement Scaling at One-Dimensional Quantum Critical Points, Phys. Rev. Lett. **102**, 255701 (2009).

[75] B. Pirvu, G. Vidal, F. Verstraete, and L. Tagliacozzo, Matrix product states for critical spin chains: Finite-size versus finite-entanglement scaling, Phys. Rev. B **86**, 075117 (2012).

[76] C. Liu, L. Wang, A. W. Sandvik, Y.-C. Su, and Y.-J. Kao, Symmetry breaking and criticality in tensor-product states, Phys. Rev. B **82**, 060410 (2010).

[77] F. Verstraete, M. M. Wolf, D. Pérez-García, and J. I. Cirac, Criticality, the Area Law, and the Computational Power of Projected Entangled Pair States, Phys. Rev. Lett. **96**, 220601 (2006).

[78] See Supplemental Material at http://link.aps.org/supplemental/10.1103/PhysRevB.96.014414 for the classification of all SU(2)-invariant $S = 1/2$, $D = 7$ tensors and expressions of all 30 $A_1 D = 7$ tensors.

[79] W. H. Press, S. A. Teukolsky, W. P. Vetterling, and B. P. Flannery, *Numerical Recipes* (Cambridge University Press, Cambridge, 2007).

[80] T. Nishino, K. Okunishi, and M. Kikuchi, Numerical renormalization group at criticality, Phys. Lett. A **213**, 69 (1996).

[81] N. D. Mermin and H. Wagner, Absence of Ferromagnetism or Antiferromagnetism in One- or Two-Dimensional Isotropic Heisenberg Models, Phys. Rev. Lett. **17**, 1133 (1966).

[82] A. W. Sandvik and R. Moessner, Correlations and confinement in nonplanar two-dimensional dimer models, Phys. Rev. B **73**, 144504 (2006).

[83] J. Lou, A. W. Sandvik, and N. Kawashima, Antiferromagnetic to valence-bond-solid transitions in two-dimensional SU(N) Heisenberg models with multispin interactions, Phys. Rev. B **80**, 180414 (2009).